Journal of Energy Storage 150 (2026) 120376

Contents lists available at ScienceDirect

Journal of Energy Storage

journal homepage: www.elsevier.com/locate/est

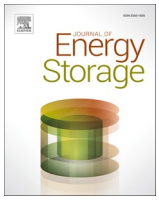

Research Papers

Implementation of gas formation into a finite-element model for the mechanical swelling simulation of lithium-ion batteries

Jun Yin [a,*], Christoph Drießen [a], Rico Klink [b,c], Stephan Kizio [b], Jörg Moser [a], Christian Ellersdorfer [a], Patrick Höschele [d]

[a] Vehicle Safety Institute, Graz University of Technology, Inffeldgasse 13, 8010, Graz, Austria
[b] AUDI AG, Neckarsulm, Germany
[c] Institute of Applied Materials — Electrochemical Technologies (IAM-ET), Karlsruhe Institute of Technology (KIT), Adenauerring 20b, Karlsruhe, Germany
[d] Battery4Life GmbH, Inffeldgasse 23/1, 8010, Graz, Austria

ARTICLE INFO

Keywords:
Lithium-ion battery
Prismatic cell
Gas formation
Swelling
Mechanical simulation
CT scan

ABSTRACT

Lithium-ion batteries (LIBs) are playing an increasingly vital role in electric vehicles. LIBs are assembled into modules with a preload force to ensure stability and safety. During cycling, battery swelling increases the force within the module. In addition, gas formation, resulting from the battery aging mechanisms, may impact swelling behavior and impair battery performance and safety. While researchers have developed various models to analyze swelling mechanisms, few have considered implementing gas formation into mechanical swelling models. However, the effect of gas formation should not be overlooked, as it has a significant impact on aged batteries. Herein, we implement gas formation into a simplified finite element model to better evaluate the swelling mechanism of LIBs. We found that, for the model of an aged cell with 1900 cycles, it achieves a mean absolute percentage error (MAPE) of 10.24% for force change and 15.12% for thickness change with gas formation (as compared with experimental results), versus the 565.05% for force change and 228.30% for thickness change achieved without gas formation, thus underscoring the critical impact of gas formation on cell swelling mechanisms. These findings suggest that gas formation is a needed consideration in a swelling model to predict a change in battery thickness and swelling-related force fluctuation. The approach in our study is crucial for evaluating the impact of gas on battery mechanical behavior and can be applied to determine the optimal preload force in further investigations.

1. Introduction

Lithium-ion batteries (LIBs) are widely used as energy storage systems (ESSs) in electric vehicles (EVs) due to their high energy density and efficiency. However, battery aging occurs during operation in ESSs: this causes gas formation through electrolyte breakdown and side reactions, producing gases such as CO, CO_2, H_2, and CH_4 [1]. This gas formation increases internal pressure, leading to structural damage such as electrode cracking, delamination, and casing deformation [1]. It also impacts swelling behavior, particularly in constrained systems, where increased mechanical stress heightens the risk of failures such as internal short circuits [2–4]. Analyzing the effect of gas formation on mechanical behavior is therefore critical for understanding swelling dynamics, ensuring structural integrity, and designing safer battery systems for real-world applications over the whole lifecycle.

The swelling of LIBs occurs throughout their lifetime, specifically during cycling, and can be classified into reversible and irreversible types [3,5,6]. Reversible swelling results from the expansion and contraction of composite electrodes due to the effects of insertion, alloying and conversion [7–9]. Irreversible swelling arises from side reactions such as SEI growth and gas generation, plastic deformation, and mechanical damage [10–12]. Both types affect battery lifespan and performance [13–16]. LIB cells for automotive application are assembled into modules or cell-to-pack systems with an equivalent functionality of the pack housing to ensure stability and safety, with housings designed to resist external and internal mechanical stresses [6,17,18]. The initial preload force of the housing is optimized to enhance battery performance and influences internal pressure over the battery lifetime [19,20]. Under specific preload force, the swelling of LIBs increases housing pressure during cycling, which may affect performance and the

* Corresponding author.
E-mail address: jun.yin@tugraz.at (J. Yin).

https://doi.org/10.1016/j.est.2026.120376
Received 8 October 2025; Received in revised form 19 December 2025; Accepted 3 January 2026
Available online 12 January 2026

cycle life [21,22].

Researchers use various models to analyze the swelling mechanisms in LIBs, including particle-level, electrode-level, and full-battery finite element models [9,23–26]. Using electron microscopy observations, Yang et al. [27] created an anisotropic model to describe particle swelling and cracking. Leo et al. [28] developed a phase-field model to study particle-level swelling, thus revealing microstructural changes during battery swelling. Garrick et al. [29] developed a coupled electrochemical mechanical model to quantify the aging-induced irreversible volume change of porous electrodes. These models effectively capture reversible and irreversible swelling mechanisms caused by electrode expansion and structural changes due to lithium intercalation and material degradation. However, the current models do not include gas formation in swelling predictions, despite the significant role it plays in aged batteries. Gas formation from electrolyte breakdown and side reactions increases internal pressure, potentially leading to structural damage and consequently affecting battery performance and safety [30,31]. This limitation reduces the accuracy of existing models in predicting the swelling mechanisms of aged batteries.

This study aims to implement gas formation into a finite element model to better evaluate the swelling mechanism of LIBs. The main goal is thus to improve the prediction quality of a numerical model for swelling and external force by incorporating the physics of gas formation alongside solid swelling mechanisms. We conduct gas expansion aging experiments and perform CT-scan analyses to investigate the internal cell structure. Moreover, validation tests are conducted in a constrained setup to simulate real-world operating conditions. The research findings enable us to estimate the impact of gas on cell swelling and fluctuations in external force during cycling.

2. Methods

2.1. Specimen

The study used commercial NCA/graphite lithium-ion prismatic cells with a nominal capacity of 70 Ah. An overview of the cell specifications is given in Table 1. The fresh prismatic cell had a dimension of 220 × 100 × 21.3 mm, which describes the average thickness of the cell at a 0% state of charge (SOC).

For the analysis, three cells with three different aging histories, referred to as fresh cell, aged cell 1 and aged cell 2, are utilized in the study, see Table 2. The fresh cell experienced minimal electrical cycling compared with aged cell 1 and aged cell 2, which underwent 200 and 1900 cycles respectively. Aged cell 1 is aged at 25 °C using a cycling protocol between 100% and 0% SOC, as specified in Table 3. The whole procedure includes four steps: constant current-constant voltage (CC-CV) charging, relaxation after charging, constant current (CC) discharging and relaxation after discharging. Aged cell 2 is aged with 1 C at 35 °C in a climate chamber using CC-CV charging and CC discharging between 97% and 8% SOC. The cell capacity is measured every 100 cycles by determining the OCV voltage corresponding to 97% SOC. For aged cell 1, the aging procedure is more intensive, in order to accelerate the gas formation within a limited number of cycles. For aged cell 2, the aging procedure is designed to reflect gas formation under realistic long-term cycling conditions. These two distinct aging protocols are employed to generate contrasting levels of gas formation within a feasible experimental timeframe. Aged cell 1 underwent an accelerated aging protocol with repeated full cycles to provoke intensive electrolyte decomposition and noticeable gas generation in 200 cycles. In contrast, aged cell 2 followed a realistic automotive cycling protocol, which produced obvious and more severe gas formation under long-term operating conditions. This contrast enables direct comparison of mechanical behavior between cells with moderate gas formation from short-term accelerated aging and cells exhibiting severe gas evolution after long-term realistic cycling.

Table 1
Basic data of fresh specimen.

Parameter	Value
Nominal capacity	70 Ah
Dimension	220 × 100 × 21.3 mm
Cathode/anode material	NCA/graphite
Max. operating voltage (current 1 C)	4.15 V
Min. operating voltage (current 1 C)	3 V

Table 2
Aging histories of tested cells.

Cell	Number of cycles	SOH (%)
Fresh cell	3	100.00
Aged cell 1	200	94.52
Aged cell 2	1900	76.61

Table 3
Cycling procedure specification.

Step	Control type	Control value
1	CC-CV charging	CC phase charging current 70 A, cut-off voltage 4.15 V, CV phase cut-off current 3.5 A
2	Charging relaxation	30 min
3	CC discharging	CC phase discharging current 70 A, cut-off voltage 3 V
4	Discharging relaxation	30 min

2.2. Test setup and experimental procedure

An unconstrained and a constrained test setup are developed separately in this study, as illustrated in Fig. 1. The unconstrained setup is designed to measure cell thickness change during cycling with two high-precision capacitive sensors (Micro-Epsilon CSE3), as shown in Fig. 1(a). Each capacitive sensor has an accuracy of ±0.012 µm. The distance between the two sensors is measured before the test as a reference value to calculate the cell thickness. The cell thickness is calculated from the distance of d_1 and d_2, as measured by the two capacitive sensors during cycling. The constrained setup is designed to apply controlled force to the cell surface as shown in Fig. 1(b). The test setup consists of four steel plates (labeled Top Plate 1, Top Plate 2, Bottom Plate 1 and Bottom Plate 2), which are connected by four bolts and hexagon nuts on the edges. A disk spring (DIN 2093, 125 mm outer diameter, 71 mm inner diameter, 8 mm thickness) is placed between Top Plate 1 and Top Plate 2 to account for a realistic bracing. The overall stiffness of the test setup is chosen to be 25 kN/mm, representing the stiffness of the cell integration setup in the battery application. The battery cell is placed between Top Plate 2 and Bottom Plate 1. Two displacement sensors, identical to those used in the unconstrained setup, are attached on the edges of Top Plate 2 to measure the change in thickness of the cell during cycling. A load cell of 25 kN (GTM Series K) is placed between Bottom Plate 1 and Bottom Plate 2 to measure the compression force.

The fresh cell, aged cell 1, and aged cell 2 are tested under two conditions: unconstrained without applied preload force (0 kN) and constrained with a preload force of 1.5 kN at 30% SOC. The experimental procedure is shown in Fig. 2. Each procedure is repeated three times with one sample of a fresh cell, aged cell 1, and aged cell 2 sample. For the unconstrained test, only the change in cell thickness is measured. For the constrained test, both the change in cell thickness and the compression force are measured.

For the unconstrained case, the cell is first cycled three times using the same CC-CV charging protocol and CC discharging protocols, as specified in Table 3. After the three cycles, the cell is charged using the same CC-CV charging protocol from 0% to 100% SOC, as specified in

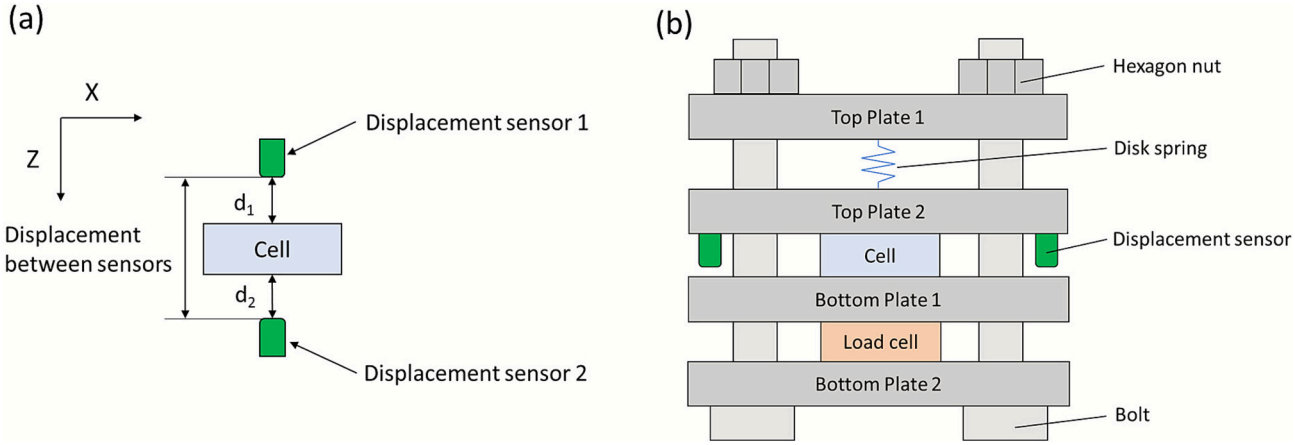

Fig. 1. Schematic drawings of the test setup: (a) cell thickness measurement in the unconstrained setup, (b) cell thickness and force measurement in the constrained setup.

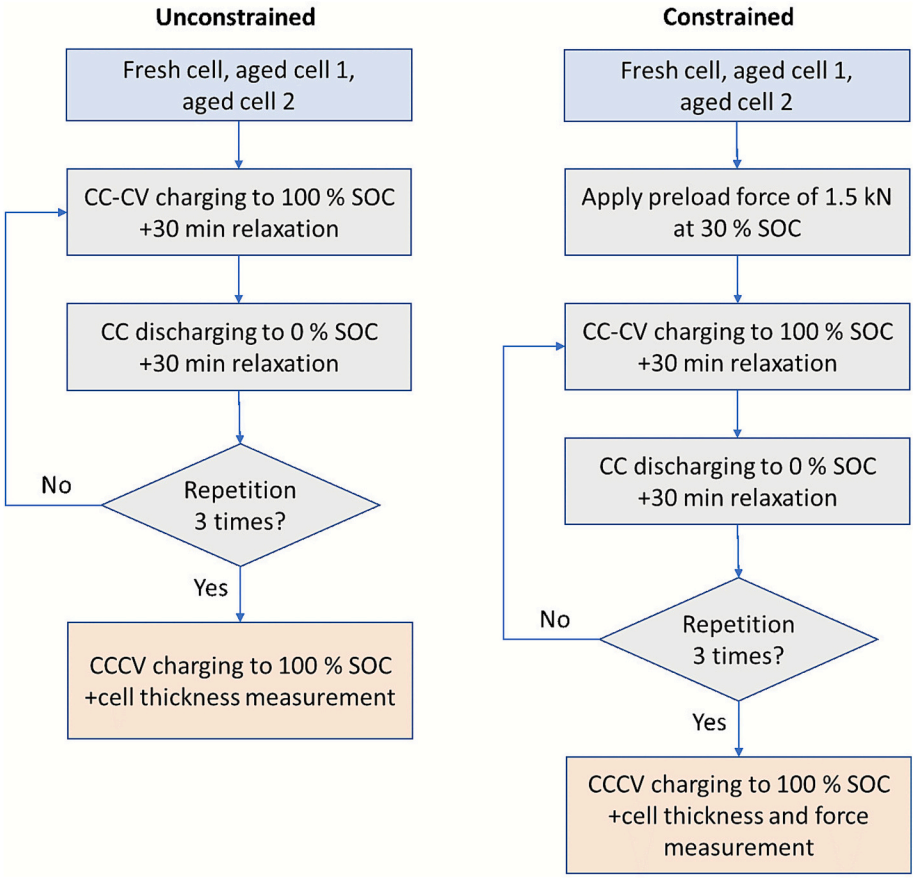

Fig. 2. Experimental procedure with/without preload force.

Table 3. The cell thickness is measured during cycling.

For the constrained case, a preload force of 1.5 kN is applied at 30% SOC in order to represent the mechanical constraint during the battery module manufacturing process. After applying the 1.5 kN preload force, the cell is cycled three times using the same CC-CV charging and CC discharging protocols as specified in Table 3. Following cycling, the preload force is expected to decrease due to mechanical relaxation, which becomes stable at the end of the cycling process. The stabilized force serves as the baseline value for subsequent measurements of cell thickness and force. After the three cycles, the cell is charged using the same CC-CV charging protocol from 0% to 100% SOC, as specified in Table 3. The cell thickness and force are measured during cycling.

2.3. CT scan

A lab-based X-ray computed tomography (CT) scanner (TESCAN UniTOM HR) is used to investigate and visualize the internal cell structure. The goal is to estimate the amount of gas formation inside the cell due to aging. CT scans are conducted on three cells: fresh cell, aged cell 1, and aged cell 2. During the scanning process, each cell is at 0% SOC. The scans utilize a CT scanner set to a voltage of 180 kV, with a power output of 94.2 W and a target current of 523 μA. The exposure

time is 140 ms per scan, with the device configured in stamina vertical mode. A workflow of the CT-scan analysis and a parameter table is added in Appendix A. Work flow and parameters of CT-scan analysis.

2.4. Finite element model

A finite element model is developed using LS-DYNA software to simulate cell swelling. The finite element cell model is created by a casing part and a jelly stack part, illustrated in Fig. 3. Fig. 3(a) shows the casing part with shell section and material MAT_ELASTIC. The casing material is simulated using the mechanical properties of aluminum 3003-H14, as specified in the manufacturer's cell data sheet. Fig. 3(b) shows the jelly stack part with solid section, material *MAT_HONEYCOMB and MAT_ADD_THERMAL_EXPANSION. The honeycomb model is suitable for describing materials with real anisotropic behavior, such as foam and honeycomb materials. Höschele et al. [32] shows that jelly stack could be simulated as a hexagonal honeycomb. Reversible swelling is modeled using thermal expansion and is calibrated with fresh cell data from 0% to 100% SOC during the charging phase. In our study, we focus specifically on thickness-direction swelling behavior under constrained conditions. Since the primary deformation occurs in the through-thickness direction and in-plane swelling is negligible [33], we simplified the anisotropic parameters by assuming equivalent compression and shear moduli in the x, y, and z directions. This approach captures the dominant mechanical response while maintaining computational efficiency. The mechanical parameters for the honeycomb material are shown in Table 4. The Young's modulus at full compaction E and the Poisson's ratio υ are specified as 4.80 GPa and 0.1, respectively. The relative volume at full compaction for the elements V_f is selected as 0.3. For the uncompressed material, the Young's moduli E_{iiu} and shear moduli G_{iju} are uniformly defined as 2.68 GPa in all material directions.

A preliminary simulation is performed using AIRBAG_LOAD_CURVE_ID with a prescribed pressure-versus-time curve. The simulation is run until the inflated airbag dimension matches the measured displacement between the casing and the jelly stack from CT-scan analysis. The gas volume is then calculated based on the simulation results. At this point, the resulting equilibrium gas pressure is extracted as the calibrated internal gas pressure consistent with the observed cell swelling. The airbag is defined using SET_SEGMENT containing shell section and outer surface of solid section. The normal vectors of this segment are defined as pointing outwards from the airbag. The control volume of the airbag is between the shell and the solid cross-section. Gas formation is simulated using AIRBAG_SIMPLE_AIRBAG_MODEL, with gas amounts calculated from the CT scan data of aged cells at 0% SOC according to Eq. (1). In this equation, the mass of gas m_{gas} is calculated by applying the ideal gas law. The pressure of gas P_{gas} is calibrated by LS-DYNA to match the same geometrical data of the internal cell structure. The V_{gas} is the gas volume between the jelly stack and casing based on CT-scan results and M_{gas} represents the gas molar mass. The gap between the casing and the jelly stack extracted from CT scan represents the total accumulated gas within the cell. This geometrical feature is incorporated through the airbag component, which is positioned between the jelly stack and the casing to represent the gas pocket. In our study, the gas is assumed to exhibit the properties of air in order to simplify the overall simulation process. We acknowledge that the air assumption introduces uncertainty in absolute pressure values. However, the research on qualitative mechanical behavior patterns remain instructive for understanding gas swelling effects on prismatic cell mechanics.

Table 4
Material parameters for a honeycomb material.

Parameter					
ρ (kg/mm^3)	E (GPa)	ν (–)	V_f (–)	E_{iiu} (GPa)	G_{iju} (GPa)
2.6×10^{-6}	4.80	0.1	0.3	2.68	2.68

$$m_{gas} = \frac{P_{gas} V_{gas}}{RT} \bullet M_{gas} \quad (1)$$

A constrained model is implemented in LS-DYNA to validate the effect of gas on cell swelling with preload force, as shown in Fig. 4. The cell is constrained with a steel top plate and a bottom plate. A spring element and a damper element are connected to the top plate to apply force on the cell. The top and end plates are created with a solid section and steel material properties. In this study, the simulation assumes a homogeneous force distribution across the finite element cell stack in order to simplify the computational analysis while preserving the mechanical behavior of the stacked cell design.

The charging phase of the constrained aged cell 1 and aged cell 2 is simulated to validate the effect of gas formation on swelling behavior. The simulation procedure is shown in Fig. 5. For each case, the constrained swelling is simulated separately with gas formation and without gas formation.

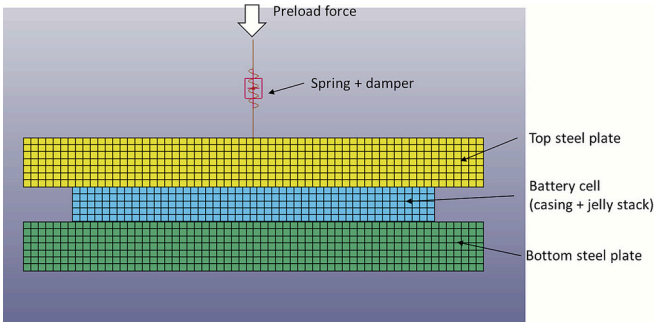

Fig. 4. Constrained finite element model.

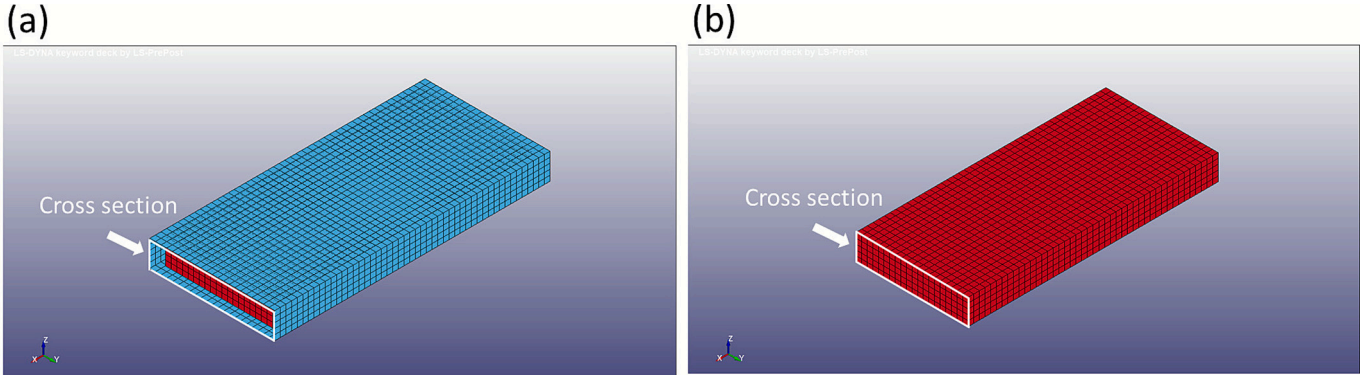

Fig. 3. Finite element model in LS-DYNA; (a) casing part and (b) jelly stack.

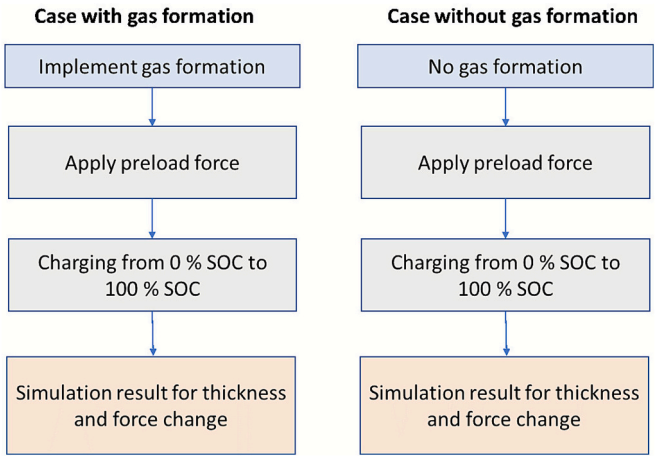

Fig. 5. Simulation procedure with/without gas formation.

3. Results

3.1. Experimental results

The experimental result for the unconstrained and constrained cases of 1.5 kN preload force during the charging phase is shown in Fig. 6. The curves in Fig. 6 present the average data from three repeated experiments. Fig. 6(a) shows that the cell thickness increases by 0.353 mm, 0.677 mm and 0.776 mm from 0% to 100% SOC for the fresh cell, aged cell 1 and aged cell 2 respectively in the unconstrained case. For all three cells, the maximum change in cell thickness occurs between the SOC range of 80% and 90%. The thickness change decreases slightly after reaching the maximum value. Fig. 6(b) shows that the force change is smaller for aged cells 2 during the charging phase compared with the fresh cell and aged cell 1. The end force change is 4103 N, 2629 N and 353 N for the fresh cell, aged cell 1 and aged cell 2 respectively. Fig. 6(c) shows that the cell thickness changes of aged cells are smaller than for the fresh cell. The cell thickness change at 100% SOC is 0.194 mm, 0.124 mm and 0.039 mm for the fresh cell, aged cell 1 and aged cell 2 respectively. According to Niu et al. [34], the cell compression modulus decreases due to the effect of aging. Our study hypothesizes that gas formation, resulting from cell aging, is a key factor contributing to the reduction of the cell compression modulus. The internal gas may function as a compressible medium, reducing the cell's mechanical stiffness by mitigating the impact of jelly stack expansion. Consequently, this effect results in less change in thickness and force fluctuation during cycling under the same mechanical constraint. The statistical analysis, including maximum and minimum measurements, is presented in Appendix B. Statistical analysis of experimental results.

3.2. CT scan results

We clarify that CT-scan analysis in this study is conducted primarily to visualize and characterize the internal cell structure rather than to extract gas volume directly through reconstruction and segmentation of imaging data. We then measure the physical displacement between the jelly stack and the battery casing, as this gap region represents where the generated gas is distributed within the cell.

CT scan results reveal the internal structure of the cell including an

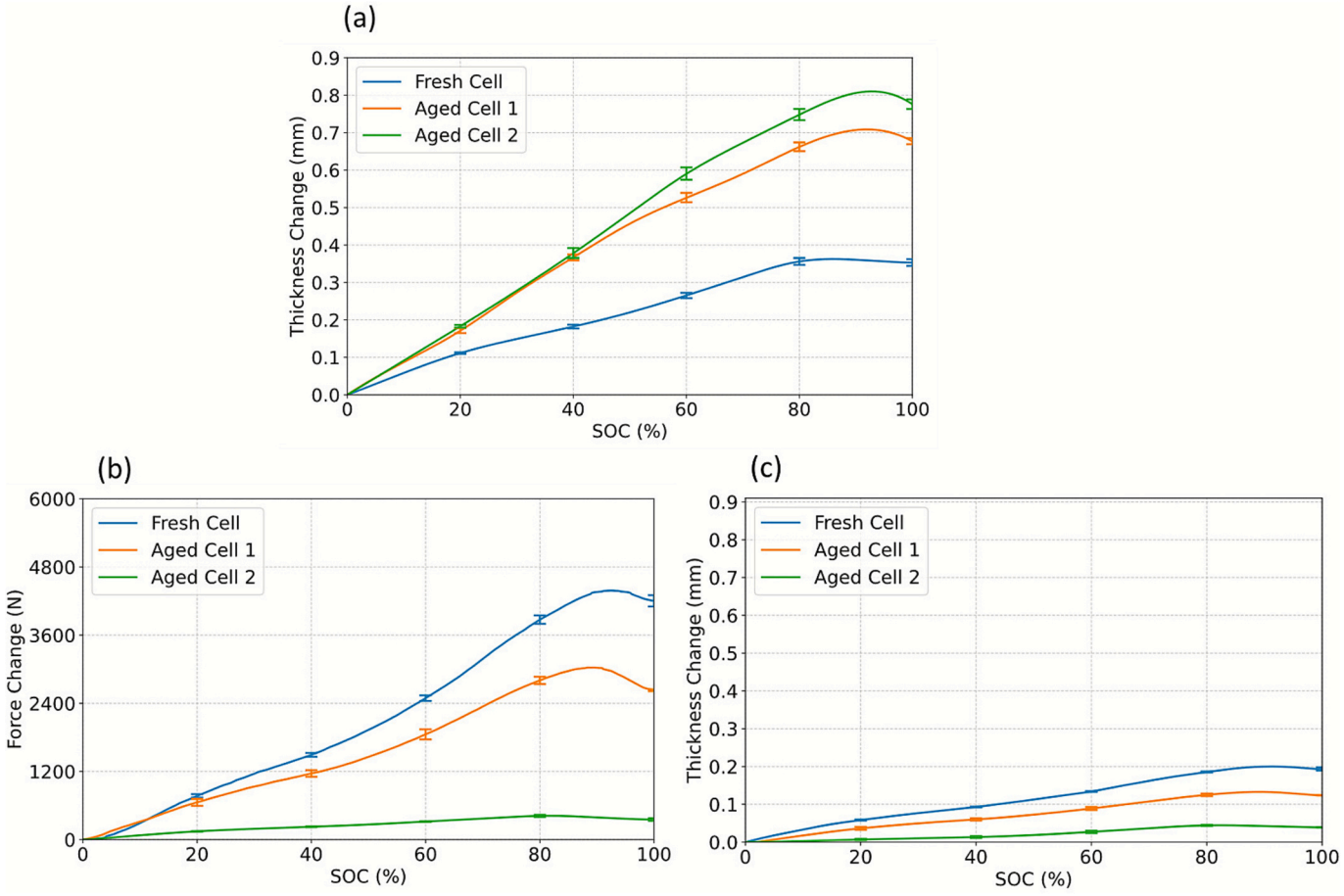

Fig. 6. Experimental results for unconstrained and constrained cases during the charging phase: (a) change in thickness for the unconstrained case, (b) force change for the constrained case of 1.5 kN preload force, (c) change in thickness for the constrained case of 1.5 kN preload force.

overview of the casing, jelly stack and distribution of electrode layers, as shown in Fig. 7. There is almost no gap between the jelly stack and casing in the fresh cell from Fig. 7(a), a slight gap of 0.37 mm in the aged cell 1 from Fig. 7(b), and a clear gap of 3.28 mm in the aged cell 2 from Fig. 7(c). A larger gap indicates that there is more gas formation in cells with more intensive aging.

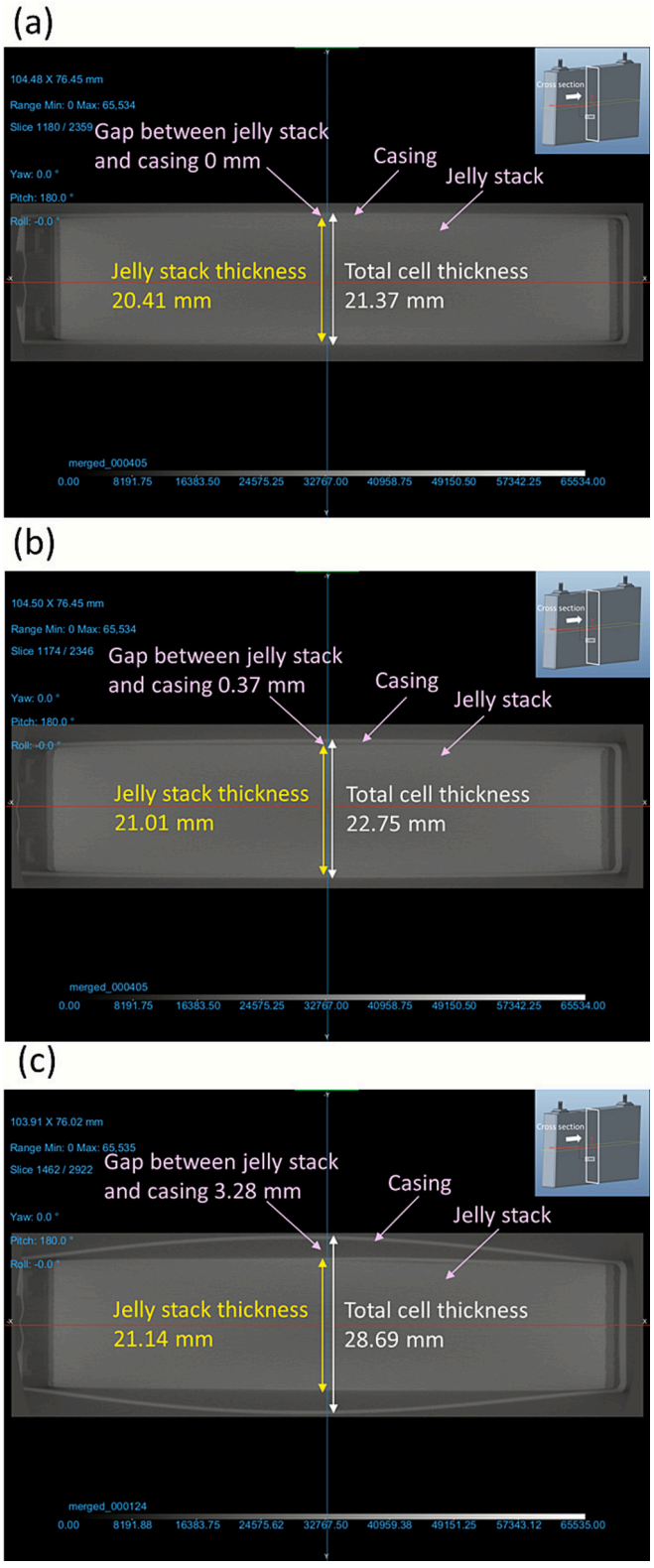

Fig. 7. CT scan result for the fresh cell, aged cell 1 and aged cell 2: (a) CT cross-section for fresh cell, (b) CT cross-section for aged cell 1, (c) CT cross-section for aged cell 2.

Cell thickness data from CT scan results are summarized in Table 5. The jelly stack and total cell thickness are measured from the cell center point using analysis software for CT results. Based on the result of the CT scan, we assume there is no gas in the fresh cell for subsequent simulations as a negligible gap is observed between the jelly stack and casing.

The jelly stack thickness increases by 2.94% for aged cell 1 and 3.58% for aged cell 2 compared with the fresh cell, which can be attributed to irreversible swelling. Total cell thickness increases by 6.46% for aged cell 1 and 34.25% for aged cell 2, primarily due to gas formation.

3.3. Model calibration results

3.3.1. Jelly stack expansion

The thermal expansion coefficient of the jelly stack is derived from the thickness change curve of the fresh cell in an unconstrained case, as shown in Fig. 8. In LS-DYNA, the thermal expansion coefficient curve was loaded into the keyword module MAT_ADD_THERMAL_EXPANSION. In Fig. 8(a), a temperature curve is set from 0 °C to 100 °C that represents SOC from 0% to 100% during the charging phase. The Y-axis in Fig. 8(a) is the thermal expansion coefficient with unit $°C^{-1}$. It represents the strain change of the jelly stack with SOC (temperature in LS-DYNA instead). The SOC-to-temperature mapping function is directly calibrated from experimental data shown in Fig. 8 (a). The thermal expansion coefficient curve represents the reversible mechanical expansion behavior characteristic of NCA battery cells during charging. For aged cells, our experimental observations and findings from literature [32] indicate that the reversible swelling behavior remains relatively consistent across different aging conditions, and we do not expect significant differences in the SOC-swelling relationship. Therefore, the calibrated mapping function can be reasonably applied across various aging states. The comparison of the thickness change of the test and simulation for fresh cell expansion during the charging phase is shown in Fig. 8(b). The model predicts the jelly stack thickness change of a fresh cell from 0 mm to 0.353 mm. Experimental results show an increase from 0 mm to 0.354 mm. The mean absolute percentage error (MAPE) between the experimental and simulation data is 3.66%. The calibrated jelly stack expansion result is applied to the fresh cell, aged cell 1, and aged cell 2 for model validation. Here we assume that the solid swelling of the jelly stack is the same for fresh and aged cells. The assumption of constant solid swelling represents a first-order approximation that enables us to isolate the impact of gas generation on the mechanical properties of the cell while neglecting potential aging-induced changes in electrode expansion characteristics.

3.3.2. Gas implementation

For aged cell 1, gas mass increased from 0 g to 0.0227 g as calculated based on the Eq. (1). The model predicted total cell thickness increasing from 21.30 mm to 22.62 mm compared with the CT scan result of 22.75 mm, as shown in Table 6. The MAPE for cell thickness between the simulation and CT scan result is 0.57%.

For aged cell 2, gas mass increased from 0 g to 0.2143 g as calculated based on the Eq. (1). The model predicted total cell thickness increasing

Table 5
Cell thickness measurements from CT scan results.

Cell	Jelly stack thickness (mm)	Total cell thickness (mm)	Gap between jelly stack and casing (mm)
Fresh cell	20.41	21.37	0
Aged cell 1	21.01 (+2.94%)	22.75 (+6.46%)	0.37
Aged cell 2	21.14 (+3.58%)	28.69 (+34.25%)	3.28

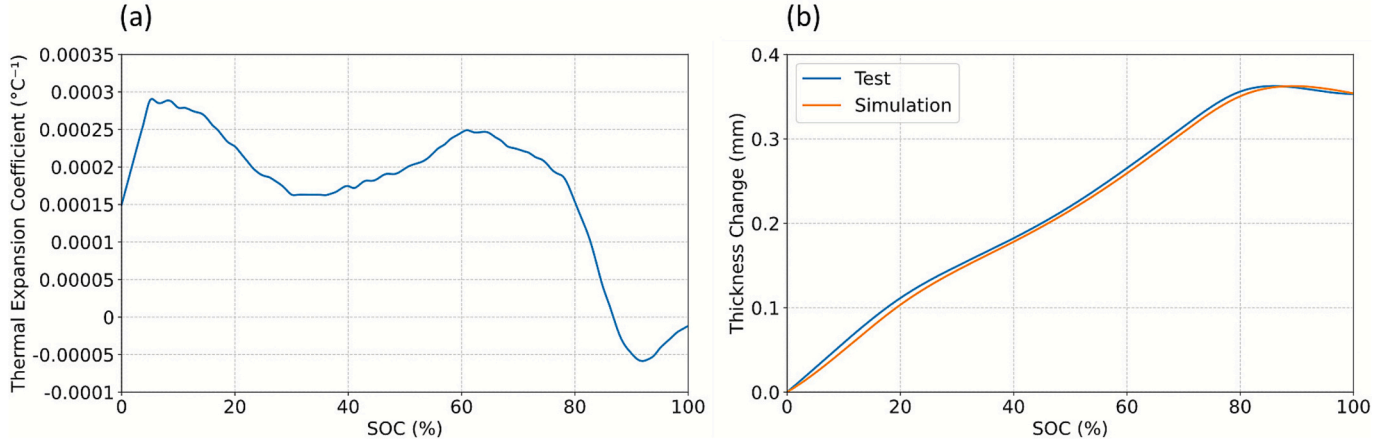

Fig. 8. Calibration of jelly stack expansion of an unconstrained fresh cell during the charging phase: (a) thermal expansion coefficient of jelly stack, (b) comparison of the change in cell thickness between test and simulation.

Table 6
Maximum cell thickness simulation results.

Cell	Maximum cell thickness from CT scan (mm)	Maximum cell thickness from simulation (mm)	MAPE for cell thickness between CT scan and simulation (%)
Aged cell 1	22.62	22.75	0.57
Aged cell 2	28.50	28.69	0.66

from 21.30 mm to 28.50 mm, compared with the CT scan result of 28.69 mm, as shown in Table 6. The MAPE for cell thickness between the simulation and CT scan result is 0.66%.

3.4. Model validation results

The simulation result of the constrained swelling of a fresh cell is shown in Fig. 9(a) and (b). The model shows a MAPE of 9.31% for force change and 2.72% for thickness change (compared with experimental results).

The simulation result of the constrained swelling of aged cell 1 is shown in Fig. 9(c) and (d). The model with gas shows a MAPE of 10.64% for force change and 8.05% thickness change (compared with experimental results). Without gas, the MAPE is 25.84% for force change and 16.64% for thickness change. The simulation results indicate that gas formation in aged cell 1 impacts mechanical behavior. The cell stiffness decreases slightly due to the gas formation, which results in reduced thickness and force increase during the charging phase (compared with the case without gas).

The simulation result of the constrained swelling of aged cell 2 is shown in Fig. 9(e) and (f). The model with gas shows a MAPE of 10.24% for force change and 15.12% for thickness change (compared with experimental results). Without gas, the MAPE is 565.05% for force change and 228.30% for thickness change. The simulation results indicate that gas formation in aged cell 2 significantly affects its mechanical behavior. The gas mass in aged cell 2 is 9.44 times more than in aged cell 1. Therefore, the impact of gas formation on cell stiffness is more obvious in aged cell 2, leading to a MAPE of 571.02% for force change and 251.57% for thickness change (compared with the case without gas formation).

All simulations are performed on a local workstation (Windows 10 Enterprise 64-bit, Intel Core i7-10700K CPU with 8 cores at 3.80 GHz) using LS-PrePost Version 4.6-x64 for pre- and post-processing. The average simulation time is 10 min 54 s without gas formation and 13 min 12 s with the airbag model activated, representing a 21% increase in computational cost. This additional overhead stem primarily from airbag thermodynamics calculations and contact algorithms. Given the improvement in prediction accuracy for aged cell mechanical response, we consider this moderate computational penalty acceptable for large-scale simulations.

4. Conclusion

This study has developed a finite element model that integrates gas formation with solid swelling mechanisms to evaluate swelling and external force fluctuation in LIBs. The model improves the prediction accuracy of cell swelling under constrained conditions, filling a critical gap in the lack of gas formation impact for existing swelling models.

Experimental results highlight the impact of gas formation on cell stiffness. CT scan results show larger gaps in aged cells, with aged cell 2 exhibiting a 34.25% increase in total cell thickness due to gas accumulation, compared with 6.46% for aged cell 1. In the charging phase of the unconstrained case, the change in cell thickness is 0.353 mm, 0.677 mm and 0.776 mm for the fresh cell, aged cell 1, and aged cell 2, respectively. In the charging phase of the constrained case with 1.5 kN preload force, thickness change is 0.124 mm for aged cell 1 and 0.039 mm for aged cell 2, versus 0.194 mm for the fresh cell, with a force change of 2629 N for aged cell 1 and 353 N for aged cell 2 (compared with 4101 N for the fresh cell). Our study hypothesizes that gas formation is a key factor in reducing cell compression modulus, resulting in less thickness change and force fluctuation during the charging phase for aged cells.

Implemented in LS-DYNA, the model uses thermal expansion for reversible swelling and an airbag model for gas formation, which is calibrated based on CT scan data. It accurately predicts the solid swelling of the fresh cell with a MAPE of 3.66% during the charging phase. For calibration of gas formation in aged cells, the MAPE of the cell thickness is 0.57% for aged cell 1 and 0.66% for aged cell 2. Validation tests under the constrained conditions with a 1.5 kN preload force demonstrate that the model with gas implementation is more accurate than the model without gas implementation. For the model of aged cell 1, it shows a MAPE of 10.64% for force change and 8.05% for thickness change with gas, versus 25.84% for force change and 16.64% for thickness change without gas. For the model of aged cell 2, it achieves a MAPE of 10.24% for force change and 15.12% for thickness change with gas, versus 565.05% for force change and 228.30% for thickness change without gas, underscoring the critical impact of gas formation for cell swelling mechanisms.

The key advantage of the model is the implementation of gas formation as an aging effect, thus improving prediction accuracy over

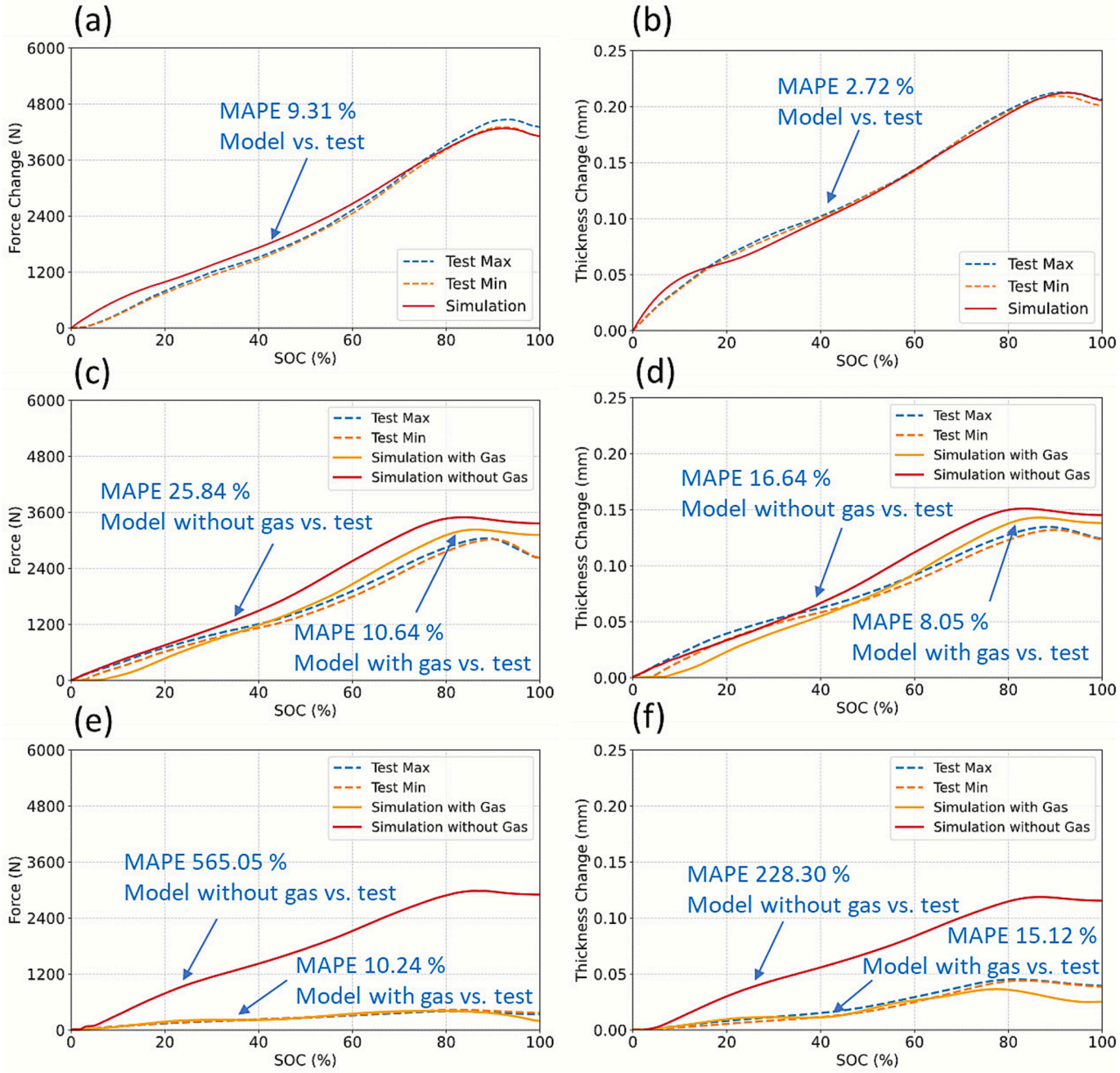

Fig. 9. Validation for the constrained case of 1.5 kN preload force during the charging phase: (a) force change for fresh cell, (b) thickness change for fresh cell, (c) force change for aged cell 1, (d) thickness change for aged cell 1, (e) force change for aged cell 2, (f) thickness change for aged cell 2.

models limited to solid swelling. Based on the simulation results, the consideration of gas formation in a swelling model is needed in order to predict cell thickness change and swelling-related force fluctuation. Our findings indicate that gas formation leads to diminished force response during cycling in aged cells. Over extended operation, the accumulation of internal gas pressure may compromise mechanical integrity and increase the risk of safety-critical failures. Understanding these aging-induced mechanical changes is essential for safety risk assessments and can inform preload optimization strategies in battery module design. This approach is crucial for evaluating gas impact on cell structure and external force during cycling. Moreover, it can be used to determine the optimal preload force and to monitor force change in further investigations, thereby mitigating risks such as deformation and thermal runaway caused by aging-induced gas accumulation.

CRediT authorship contribution statement

Jun Yin: Writing – original draft, Visualization, Validation, Methodology, Investigation, Formal analysis, Data curation, Conceptualization. **Christoph Drießen:** Writing – review & editing, Investigation, Data curation. **Rico Klink:** Writing – review & editing, Resources, Investigation, Data curation. **Stephan Kizio:** Writing – review & editing, Resources. **Jörg Moser:** Writing – review & editing. **Christian Ellersdorfer:** Writing – review & editing, Supervision. **Patrick Höschele:** Writing – review & editing, Supervision, Project administration, Conceptualization.

Declaration of Generative AI and AI-assisted technologies in the writing process

During the preparation of this work, the authors used Deepl, Grok 3 and Claude Sonnet 4 for checking grammar and spelling. After using these tools, the authors reviewed and edited the content as needed, and they take full responsibility for the content of the published article.

Declaration of competing interest

The authors declare that they have no known competing financial interests or personal relationships that could have appeared to influence the work reported in this paper.

Acknowledgments

This work was supported by Audi AG.

Appendix A. Work flow and parameters of CT-scan analysis

The workflow of the CT-scan analysis is described as below.

A.1. Projection acquisition

X-ray computed tomography scans were performed on a TESCAN UniTOM XL dynamic micro-CT system. Scans were acquired at 180 kV acceleration voltage and 94.2 W target power, using a 1.0 mm tin (Sn) pre-filter to reduce beam hardening. Each projection had an exposure time of 140 ms, with 7 frame averages for improved signal-to-noise ratio. A total of 1641 projections were collected over a full 360° rotation, resulting in isotropic voxel sizes of either 94.2 μm (standard scans).

A.2. Volume reconstruction

Raw projection data were reconstructed by using the TESCAN Panthera reconstruction software employing a standard filtered back-projection algorithm. The output consisted of a stack of 16-bit grayscale TIFF slices representing the full 3D volume of the prismatic cell.

A.3. Import and visualization

The reconstructed 16-bit TIFF stack was directly imported into the software Dragonfly 3D world. The image stack was examined slice-by-slice to identify structural features and characterize the internal cell geometry. The primary objective of this analysis was to identify and quantify the gap between the jelly stack and the casing, which corresponds to the gas accumulation region within the aged cells.

A.4. Gap measurement

The generated gas volume was not quantified by segmentation of individual gas pockets. Instead, the physical displacement of the gap inside the cell structure was measured. In multiple cross-sections along the cell height, the gap distance between the outer surface of the jelly stack and the inner wall of the prismatic casing was manually measured using Dragonfly's ruler and distance tools. An average gap thickness was calculated from these measurements.

The parameters of CT scan analysis are shown in Table A1:

Table A1
Parameters of CT scan analysis.

Parameter	Value/setting	Unit
Scanner	TESCAN UniTOM XL	–
Voltage	180	kV
Power	94	W
X-ray filter	Sn 1.0	mm
Exposure time	140	ms
Number of projections	1641	Per 360°
Averages per projection	7	–

The visualization parameters for CT-scan processing in Dragonfly 3D World 2024.1 are shown in Table A2:

Table A2
Visualization parameters for CT-scan processing in Dragonfly 3D World 2024.1.

Parameter	Fresh cell	Aged cell 1	Aged cell 2
Reconstructed volume dimensions (px) W × H × D	1087 × 274 × 2359	1087 × 284 × 2346	1081 × 316 × 2922
Physical dimensions (mm) W × H × D	102.34 × 25.80 × 222.10	102.35 × 26.74 × 220.90	101.78 × 29.75 × 275.11
Voxel size (μm)	94.2	94.2	94.2
Total voxels (–)	702,599,842	724,228,968	998,143,512
Total volume (mm^3)	586,366.33	604,609.88	833,017,19

Appendix B. Statistical analysis of experimental results

Average/maximum/minimum thickness increase for fresh cell, aged cell 1, and aged cell 2 under unconstrained conditions at SOC 20%, 40%, 60%, 80%, and 100% are shown in Table B1.

Table B1
Average/maximum/minimum thickness increase for fresh cell, aged cell 1, and aged cell 2 under unconstrained conditions at SOC 20%, 40%, 60%, 80%, and 100%.

SOC (%)	Fresh cell avg/max/min thickness increase (mm)	Aged cell 1 avg/max/min thickness increase (mm)	Aged cell 2 avg/max/min thickness increase (mm)
20	0.1114/0.1136/0.1092 (±2.0%)	0.1716/0.1783/0.1649 (±3.9%)	0.1831/0.1867/0.1795 (±2.0%)
40	0.1823/0.1873/0.1773 (±2.7%)	0.3671/0.3749/0.3593 (±2.1%)	0.3787/0.3920/0.3654 (±3.5%)
60	0.2653/0.2724/0.2582 (±2.7%)	0.5267/0.5392/0.5142 (±2.4%)	0.5908/0.6072/0.5744 (±2.8%)
80	0.3561/0.3653/0.3469 (±2.6%)	0.6624/0.6740/0.6508 (±1.8%)	0.7484/0.7634/0.7334 (±2.0%)
100	0.3532/0.3622/0.3442 (±2.5%)	0.6773/0.6854/0.6692 (±1.2%)	0.7762/0.7891/0.7633 (±1.7%)

Average/maximum/minimum force increase and thickness increase for fresh cell, aged cell 1, and aged cell 2 under constrained conditions with 1.5 kN preload force at SOC 20%, 40%, 60%, 80%, and 100% are shown in Table B2 and Table B3, respectively.

Table B2
Average/maximum/minimum force increase for fresh cell, aged cell 1, and aged cell 2 under constrained conditions with 1.5 kN preload force at SOC 20%, 40%, 60%, 80%, and 100%.

SOC (%)	Fresh cell avg/max/min force increase (N)	Aged cell 1 avg/max/min force increase (N)	Aged cell 2 avg/max/min force increase (N)
20	769.75/790.76/748.74 (±2.7%)	655.88/698.71/613.06 (±6.5%)	145.40/147.60/143.20 (±1.5%)
40	1492.10/1515.26/1468.95 (±1.6%)	1165.14/1205.59/1124.69 (±3.5%)	226.25/229.81/222.69 (±1.6%)
60	2490.59/2524.86/2456.32 (±1.4%)	1853.72/1915.87/1791.58 (±3.4%)	318.24/322.21/314.26 (±1.2%)
80	3872.90/3923.98/3821.82 (±1.3%)	2803.80/2848.33/2759.27 (±1.6%)	418.71/431.33/406.09 (±3.0%)
100	4203.92/4303.83/4104.01 (±2.4%)	2629.39/2660. 94/2597.84 (±1.2%)	353.60/369.31/337.90 (±4.4%)

Table B3
Average/maximum/minimum thickness increase for fresh cell, aged cell 1, and aged cell 2 under constrained conditions with 1.5 kN preload force at SOC 20%, 40%, 60%, 80%, and 100%.

SOC (%)	Fresh cell avg/max/min thickness increase (mm)	Aged cell 1 avg/max/min thickness increase (mm)	Aged cell 2 avg/max/min thickness increase (mm)
20	0.0659/0.0669/0.0648 (±1.6%)	0.0367/0.0394/0.0341 (±7.2%)	0.0069/0.0080/0.0058 (±15.9%)
40	0.1013/0.1021/0.1006 (±0.7%)	0.0603/0.0623/0.0583 (±3.3%)	0.0134/0.0136/0.0132 (±1.5%)
60	0.1430/0.1437/0.1422 (±0.5%)	0.0892/0.0918/0.0865 (±3.0%)	0.0271/0.0293/0.0250 (±8.1%)
80	0.1963/0.1972/0.1955 (±0.4%)	0.1253/0.1277/0.1229 (±1.9%)	0.0443/0.0455/0.0431 (±2.7%)
100	0.2037/0.2065/0.2009 (±1.4%)	0.1240/0.1250/0.1230 (±0.8%)	0.0391/0.0405/0.0376 (±3.7%)

Data availability

The data that has been used is confidential.

References

[1] K. Tan, W. Li, Z. Lin, X. Han, X. Dai, S. Li, Z. Liu, H. Liu, L. Sun, J. Jiang, T. Liu, K. Wu, T. Guo, S. Wang, J. Power Sources 580 (2023) 233471, https://doi.org/10.1016/j.jpowsour.2023.233471.

[2] L. Xu, S. Wang, Y. Li, Y. Li, J. Sun, F. Zhao, H. Wang, Y. Wang, C. Xu, X. Feng, Process Saf. Environ. Prot. 185 (2024) 267–276, https://doi.org/10.1016/j.psep.2024.03.011.

[3] P. Höschele, S.F. Heindl, S. Erker, C. Ellersdorfer, J. Energy Storage 65 (2023) 107228, https://doi.org/10.1016/j.est.2023.107228.

[4] M. Fasching, S. Grollitsch, P. Höschele, A. Schmid, C. Ellersdorfer, J. Energy Storage 89 (2024) 111581, https://doi.org/10.1016/j.est.2024.111581.

[5] T. Deich, S.L. Hahn, S. Both, K.P. Birke, A. Bund, J. Energy Storage 28 (2020) 101192, https://doi.org/10.1016/j.est.2020.101192.

[6] E. Michelini, P. Höschele, S.F. Heindl, S. Erker, C. Ellersdorfer, Batteries 9 (2023) 218, https://doi.org/10.3390/batteries9040218.

[7] C. Didier, W.K. Pang, Z. Guo, S. Schmid, V.K. Peterson, Chem. Mater. 32 (2020) 2518–2531, https://doi.org/10.1021/acs.chemmater.9b05145.

[8] Y. Li, Y. Lu, P. Adelhelm, M.-M. Titirici, Y.-S. Hu, Chem. Soc. Rev. 48 (2019) 4655–4687, https://doi.org/10.1039/C9CS00162J.

[9] B. Rieger, S. Schlueter, S.V. Erhard, J. Schmalz, G. Reinhart, A. Jossen, J. Energy Storage 6 (2016) 213–221, https://doi.org/10.1016/j.est.2016.01.006.

[10] L.M. Thompson, J.E. Harlow, A. Eldesoky, M.K.G. Bauer, J.H. Cheng, W.S. Stone, T. Taskovic, C.R.M. McFarlane, J.R. Dahn, J. Electrochem. Soc. 168 (2021) 20532, https://doi.org/10.1149/1945-7111/abe1da.

[11] P. Mohtat, S. Lee, J.B. Siegel, A.G. Stefanopoulou, J. Electrochem. Soc. 168 (2021) 100520, https://doi.org/10.1149/1945-7111/ac2d3e.

[12] D. Sauerteig, S. Ivanov, H. Reinshagen, A. Bund, J. Power Sources 342 (2017) 939–946, https://doi.org/10.1016/j.jpowsour.2016.12.121.

[13] V. Müller, R.-G. Scurtu, K. Richter, T. Waldmann, M. Memm, M.A. Danzer, M. Wohlfahrt-Mehrens, J. Electrochem. Soc. 166 (2019) A3796–A3805, https://doi.org/10.1149/2.1121915jes.

[14] R. Li, D. Ren, D. Guo, C. Xu, X. Fan, Z. Hou, L. Lu, X. Feng, X. Han, M. Ouyang, J. Electrochem. Soc. 166 (2019) A4106–A4114, https://doi.org/10.1149/2.0471916jes.

[15] H. Pegel, O. von Kessel, P. Heugel, T. Deich, J. Tübke, K.P. Birke, D.U. Sauer, J. Power Sources 537 (2022) 231443, https://doi.org/10.1016/j.jpowsour.2022.231443.

[16] J. Cannarella, C.B. Arnold, J. Power Sources 269 (2014) 7–14, https://doi.org/10.1016/j.jpowsour.2014.07.003.

[17] J. Cannarella, C.B. Arnold, J. Power Sources 245 (2014) 745–751, https://doi.org/10.1016/j.jpowsour.2013.06.165.

[18] T. Deich, M. Storch, K. Steiner, A. Bund, J. Power Sources 506 (2021) 230163, https://doi.org/10.1016/j.jpowsour.2021.230163.

[19] Y.H. Choi, H.K. Lim, J.-H. Seo, W.J. Shin, J.H. Choi, J.H. Park, SAE Int. J. Alternat. Power. 7 (2018) 195–205, https://doi.org/10.4271/2018-01-0439.

[20] S. Hahn, S. Theil, J. Kroggel, K.P. Birke, J. Energy Storage 40 (2021) 102517, https://doi.org/10.1016/j.est.2021.102517.

[21] Q. Wang, B. Mao, S.I. Stoliarov, J. Sun, Prog. Energy Combust. Sci. 73 (2019) 95–131, https://doi.org/10.1016/j.pecs.2019.03.002.

[22] Y. Li, S. Ding, L. Wang, W. Wang, C. Lin, X. He, eTransportation 22 (2024) 100368, https://doi.org/10.1016/j.etran.2024.100368.

[23] Y. Ali, N. Iqbal, S. Lee, Int. J. Energy Res. 45 (2021) 14788–14803, https://doi.org/10.1002/er.6754.

[24] R. Xu, Y. Yang, F. Yin, P. Liu, P. Cloetens, Y. Liu, F. Lin, K. Zhao, J. Mech. Phys. Solids 129 (2019) 160–183, https://doi.org/10.1016/j.jmps.2019.05.003.

[25] Y. Zhao, P. Stein, Y. Bai, M. Al-Siraj, Y. Yang, B.-X. Xu, J. Power Sources 413 (2019) 259–283, https://doi.org/10.1016/j.jpowsour.2018.12.011.
[26] D. Clerici, F. Mocera, A. Somà, J. Power Sources 542 (2022) 231735, https://doi.org/10.1016/j.jpowsour.2022.231735.
[27] H. Yang, F. Fan, W. Liang, X. Guo, T. Zhu, S. Zhang, J. Mech. Phys. Solids 70 (2014) 349–361, https://doi.org/10.1016/j.jmps.2014.06.004.
[28] C.V. Di Leo, E. Rejovitzky, L. Anand, J. Mech. Phys. Solids 70 (2014) 1–29, https://doi.org/10.1016/j.jmps.2014.05.001.
[29] T.R. Garrick, Y. Miao, E. Macciomei, M. Fernandez, J.W. Weidner, J. Electrochem. Soc. 170 (2023) 100513, https://doi.org/10.1149/1945-7111/acff1d.
[30] A. Giudici, J. Chapman, C. Please, J. Power Sources 640 (2025) 236553, https://doi.org/10.1016/j.jpowsour.2025.236553.
[31] S. Stock, F. Diller, J. Böhm, L. Hille, J. Hagemeister, A. Sommer, R. Daub, J. Electrochem. Soc. 170 (2023) 60539, https://doi.org/10.1149/1945-7111/acde0f.
[32] P. Höschele, C. Ellersdorfer, Batteries 9 (2023) 417, https://doi.org/10.3390/batteries9080417.
[33] P.K. Leung, C. Moreno, I. Masters, S. Hazra, B. Conde, M.R. Mohamed, R. J. Dashwood, R. Bhagat, J. Power Sources 271 (2014) 82–86, https://doi.org/10.1016/j.jpowsour.2014.07.184.
[34] Z. Niu, Z. Sun, S. Zhang, Y. Xia, J. Power Sources 641 (2025) 236884, https://doi.org/10.1016/j.jpowsour.2025.236884.